Differentiation of calcified regions and iron deposits in the ageing brain on conventional structural MR images

Original Research

Differentiation of Calcified Regions and Iron Deposits in the Ageing Brain on Conventional Structural MR Images

Maria del C. Valdés Hernández, PhD,[1–3]* Andreas Glatz, Eng,[1,3,4] Alexander J. Kiker, BMedSci,[4] David Alexander Dickie, MSc,[1,3,4] Benjamin S. Aribisala, PhD,[1–3] Natalie A. Royle, MSc,[1–3] Susana Muñoz Maniega, PhD,[1–3] Mark E. Bastin, PhD,[1–3] Ian J. Deary, PhD,[2,3,5] and Joanna M. Wardlaw, MD[1–3]

Purpose: In the human brain, minerals such as iron and calcium accumulate increasingly with age. They typically appear hypointense on T2*-weighted MRI sequences. This study aims to explore the differentiation and association between calcified regions and noncalcified iron deposits on clinical brain MRI in elderly, otherwise healthy subjects.

Materials and Methods: Mineral deposits were segmented on co-registered T1- and T2*-weighted sequences from 100 1.5 Tesla MRI datasets of community-dwelling individuals in their 70s. To differentiate calcified regions from noncalcified iron deposits we developed a method based on their appearance on T1-weighted images, which was validated with a purpose-designed phantom. Joint T1- and T2*-weighted intensity histograms were constructed to measure the similarity between the calcified and noncalcified iron deposits using a Euclidean distance based metric.

Results: We found distinct distributions for calcified regions and noncalcified iron deposits in the cumulative joint T1- and T2*-weighted intensity histograms across all subjects (correlations ranging from 0.02 to 0.86; mean = 0.26 ± 0.16; t = 16.93; $P < 0.001$) consistent with differences in iron and calcium signal in the phantom. The mean volumes of affected tissue per subject for calcified and noncalcified deposits were 236.74 ± 309.70 mm^3 and 283.76 ± 581.51 mm^3; respectively. There was a positive association between the mineral depositions ($\beta = 0.32$, $P < 0.005$), consistent with existing literature reports.

Conclusion: Calcified mineral deposits and noncalcified iron deposits can be distinguished from each other by signal intensity changes on conventional 1.5T T1-weighted MRI and are significantly associated in brains of elderly, otherwise healthy subjects.

Key Words: ageing; brain; iron; calcium; MRI; segmentation
J. Magn. Reson. Imaging 2013;00:000–000.

IRON AND CALCIUM are essential minerals for life, and occur naturally in food. However, they are also involved in several neurodegenerative mechanisms such as aggregation of proteins and metals, generation of free radicals, and oxidative stress (1). Diseases of ageing, such as Alzheimer's and Parkinson's diseases have been linked with a dysregulation in iron (2) and calcium (3) homeostasis. However, iron regulation also changes with age in normal, healthy individuals, which leads to its increased accumulation in the brain (4), and may contribute to cognitive decline (5). Cognitive ageing is an area of particular interest, given the increasing proportion of older people in society (6) (http://www.ons.gov.uk/ons/publications/index.html). There is, therefore, a need to gain further knowledge into the mechanisms of mineral accumulation in the brain, because it may provide key insights to their role in the understanding of ageing.

Recent studies have proposed assessing brain iron using a range of novel MRI techniques, such as relaxation time mapping, phase imaging, susceptibility-weighted imaging, susceptibility mapping, magnetic field correlation imaging, and direct saturation

[1]Brain Research Imaging Centre, Department of Neuroimaging Sciences, University of Edinburgh, Edinburgh, United Kingdom.
[2]Centre for Cognitive Ageing and Cognitive Epidemiology, University of Edinburgh, Edinburgh, United Kingdom.
[3]SINAPSE (Scottish Imaging Network, A Platform for Scientific Excellence) collaboration, Scotland, United Kingdom.
[4]College of Medicine and Veterinary Medicine, University of Edinburgh, Edinburgh, United Kingdom.
[5]Department of Psychology, University of Edinburgh, Edinburgh, United Kingdom.
Contract grant sponsor: The Centre for Cognitive Ageing and Cognitive Epidemiology; Contract grant number: G0700704/84698.
*Address reprint requests to: M.d.C.V.H., Brain Research Imaging Centre, Department of Neuroimaging Sciences, University of Edinburgh, Western General Hospital, Crewe Road, Edinburgh EH4 2XU, UK. E-mail: mvhernan@staffmail.ed.ac.uk
Received March 22, 2013; Accepted July 26, 2013.
DOI 10.1002/jmri.24348
View this article online at wileyonlinelibrary.com.

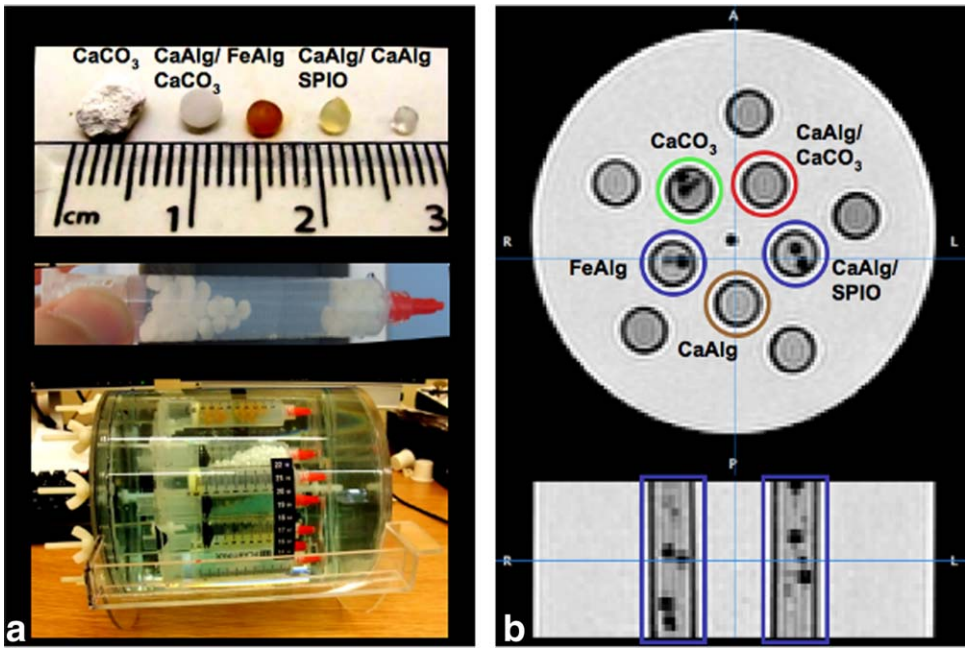

Figure 1. Phantom configuration and geometry. **a:** The models of focal calcifications and iron deposits contained $CaCO_3$, Ca^{2+}, Fe^{3+}, and Endorem (Guebert, France), and were prepared as described in the text. **b:** An axial and coronal T2*W slice of the phantom, where the five syringes containing the calcification and iron deposit models are highlighted and labeled according to the mineral model they contain. [Color figure can be viewed in the online issue, which is available at wileyonlinelibrary.com.]

imaging (7). However, these require special sequences, which may suggest longer scanning time if they are additive to a clinical scanning protocol. Additionally, some of these special sequences are unique to one manufacturer because of pending patents, have been developed for higher magnetic field strengths (3 Tesla [T] and higher) and some are sensitive to macroscopic field variations and motion, all of which limit their use in routine clinical practice (7).

Gradient echo phase images are known to offer the potential to discriminate iron from calcium (8–10), but in clinical practice they are underused. Studies report the necessity to apply postprocessing steps as one of the causes. For example, to detect small magnetic susceptibility effects using phase images, long echo times (TE) are required. However, longer TE tends to increase static field inhomogeneity effects for which a high-pass filter of a medium-sized kernel is needed (8). Another postprocessing step that often requires manual intervention is the phase unwrapping algorithm to guarantee the adequate reconstruction of the phase information (9). On the other hand, MRI scanning sequences usually require additional configuration to produce correct phase volumes, because scanners are usually optimized to produce magnitude volumes only. For example, some MRI scanners use the square root of sum-of-squares coil combination method (10) to recombine the magnitude volumes from individual coils of a phased array head coil, which is correct for obtaining the magnitude images but incorrect for obtaining the phase volumes. Postprocessing algorithms that correctly combine the individual coil images to obtain phase (11) or field maps (12) have been developed and successfully applied at the expense of large storage demands.

The aims of this study were: (i) to propose a framework to examine the relationship between mineral accumulations using imaging parameters from conventional structural MRI; (ii) to investigate the differentiation of calcified regions and noncalcified iron deposits using co-registered T1-weighted (T1W) and T2*-weighted (T2*W) MRI sequences with the hypothesis that this is achievable once calcified regions appear either hypo- or hyper-intense on T1W, noncalcified mineral deposits presumed to be iron appear isointense on T1W, and tissues with both calcium and noncalcified mineral deposits presumed to be iron appear hypointense on T2*W (5,13,14); and (iii) to examine the relationship between these regions with the hypothesis that both types of mineral accumulations correlate positively as it has been reported that the accumulation of iron tends to precede the deposition of calcium among other minerals (15).

MATERIALS AND METHODS

Validation Phantom

An MRI phantom containing calcium and iron deposit models was developed to validate the hypothesis that calcium and iron deposits, which both appear hypointense on T2*W sequences (13), can be differentiated from their appearance on T1W sequences.

The custom-built phantom (Fig. 1) consisted of a sealable, cylindrical acrylic glass container, 150 mm in diameter and 175 mm in length, in which 10 sealed 10-mL syringes (http://www.bd.com) were mounted. The syringes were uniformly distributed around two concentric circles in the plane perpendicular to the

axis of the container, and their axes were oriented parallel to the axis of the container. Each of the five syringes around the inner circle contained 5 to 10 calcium or iron deposit models of one type, which were embedded in 1.5% agarose. The five syringes around the outer circle were filled with 1.5% agarose and used as a reference. For scanning, the phantom container was filled with $CuSO_4$/NaCl solution in low concentration (16) and placed on a phantom rest that was built to fit on the GE eight-channel head coil headrest and to orient the phantom container axis parallel to the main magnetic field.

Light and heavy calcifications were modeled with calcium carbonate ($CaCO_3$) powder entrapped in gel beads and $CaCO_3$ granules obtained by grinding chalkboard sticks (Anton Franz Moertel KG, Schwabach, Germany) into pieces of 5–10 mm in diameter, respectively. $CaCO_3$ was previously proposed as a simple model for calcifications in the brain (17). Two models for light, focal calcifications were created by dripping (i) 2 % sodium alginate, 1.5 g/100 mL $CaCO_3$ solution into a 20.5 mmol/L calcium chloride solution, and (ii) 2 % sodium alginate solution into 20.5 mmol/L calcium chloride solution. This process created spherical gel beads (18) with a diameter of 1–3 mm (Fig. 1a).

Iron deposits were modeled with gel beads containing iron (Fe^{3+}) and Endorem (Guebert, France). Two models for focal iron deposits were created by dripping (i) 2% sodium alginate solution into 20.5 mmol/L iron(III) chloride hexahydrate solution, and (ii) 2% sodium alginate solution mixed with Endorem into 20.5 mmol/L calcium chloride solution. All chemicals, except chalkboard sticks and Endorem, were obtained from Sigma Aldrich (Gillingham, UK).

Subjects

We analyzed T1W and T2*W volumes from 100 participants of a study of ageing (19). Our sample (49 males and 51 females) involved community-dwelling individuals aged between 71.1 and 74.3 years (mean age = 72.7 years, SD = 0.7 years). Written informed consent was obtained from all participants under protocols approved by the Lothian (REC 07/MRE00/58) and Scottish Multicentre (MREC/01/0/56) Research Ethics Committees. All MRI scans were previously rated for mineral deposition, atrophy and white matter lesion load by an expert (J.M.W., consultant neuroradiologist with more than 25 years of experience) blinded to other details using a structured protocol (20). Images were selected based on this visual assessment to represent a full range of iron deposition, from none to many, and to include all types of these deposits, eg, brain microbleeds, deposits in the basal ganglia, midbrain, old hemorrhages, superficial siderosis, etc. We also included subjects with visual evidence of vascular disease (ie, frequent enlarged perivascular spaces, lacunes, white matter hyperintensities, cortical infarcts), as these features may affect the range of MRI intensities and have been reported to influence the accuracy of image processing techniques (21).

MRI Scans

Subjects and the phantom were imaged using a GE Signa HDxt 1.5T clinical scanner (General Electric, Milwaukee, WI) with a manufacturer supplied eight-channel phased-array head coil. For the phantom, T1W and T2*W sequences were acquired axially with a matrix of 256 × 256 and field of view (FOV) of 307 × 307 mm^2. The T1W sequence had inversion (TI), echo (TE), and repetition (TR) time values of 500/4/9.8 ms, flip angle of 8 degrees, slice thickness of 1.2 mm and bandwidth of 122 Hz/pixel. The T2*W sequence had TE/TR values of 15/940 ms, flip angle of 20 degrees, slice thickness of 2.4 mm and bandwidth of 98 Hz/pixel. Subjects were imaged following a scanning protocol fully described elsewhere (20). In this protocol, T1W and T2*W had the same acquisition parameters as those used to scan the phantom, differing only in the voxel dimensions (1 × 1 × 1.3 mm^3 for T1W and 1 × 1 × 2 mm^3 for T2*W) and in the orientation of the T1W sequence (coronal).

Preprocessing

Intensity inhomogeneities on T1W and T2W phantom images were corrected using N4 (22) from Slicer3 v3.6.3 (http://www.slicer.org). Subsequently, we registered T1W to the T2*W images using FSL FLIRT v5.5 (http://www.fmrib.ox.ac.uk/fsl/flirt/). T2*W was used as reference to minimize registration-related distortions to the hypointense areas of this sequence.

After registering the T1- and T2*-weighted subject volumes, following the same procedure as with the phantom, we automatically extracted the contents of the intracranial cavity from the T2*W sequences using the Object Extraction Tool of Analyze™ 10.0 (www.analyzedirect.com). The resulting intracranial volume (ICV) masks were visually checked and corrected when necessary following the procedure described in (23) and further applied to the T1W sequence. The extracted brains from the T1W and T2*W sequences were bias-field corrected using N4 (24).

The normal-appearing white matter was extracted using MCMxxxVI, as described and validated elsewhere (20), and the globus pallidus was extracted using FSL FIRST (http://fsl.fmrib.ox.ac.uk/fsl/fslwiki/FIRST) (25).

Mineral Segmentation

Both types of mineral depositions were automatically segmented on the T2*W brains by thresholding combined with a region-growing-based algorithm using the Object Counter Tool of Analyze™ 10.0 software). The T2*W threshold was selected relative to the T2*W intensities of the normal appearing white matter I_{NAWM} according to (26) as Eq. (1) shows:

$$Threshold = mean(I_{NAWM}) - n^* SD(I_{NAWM}) \qquad [1]$$

with $n \in \mathbf{R}^+$ as the relative threshold factor. The T2*W normal-appearing white matter intensities were used

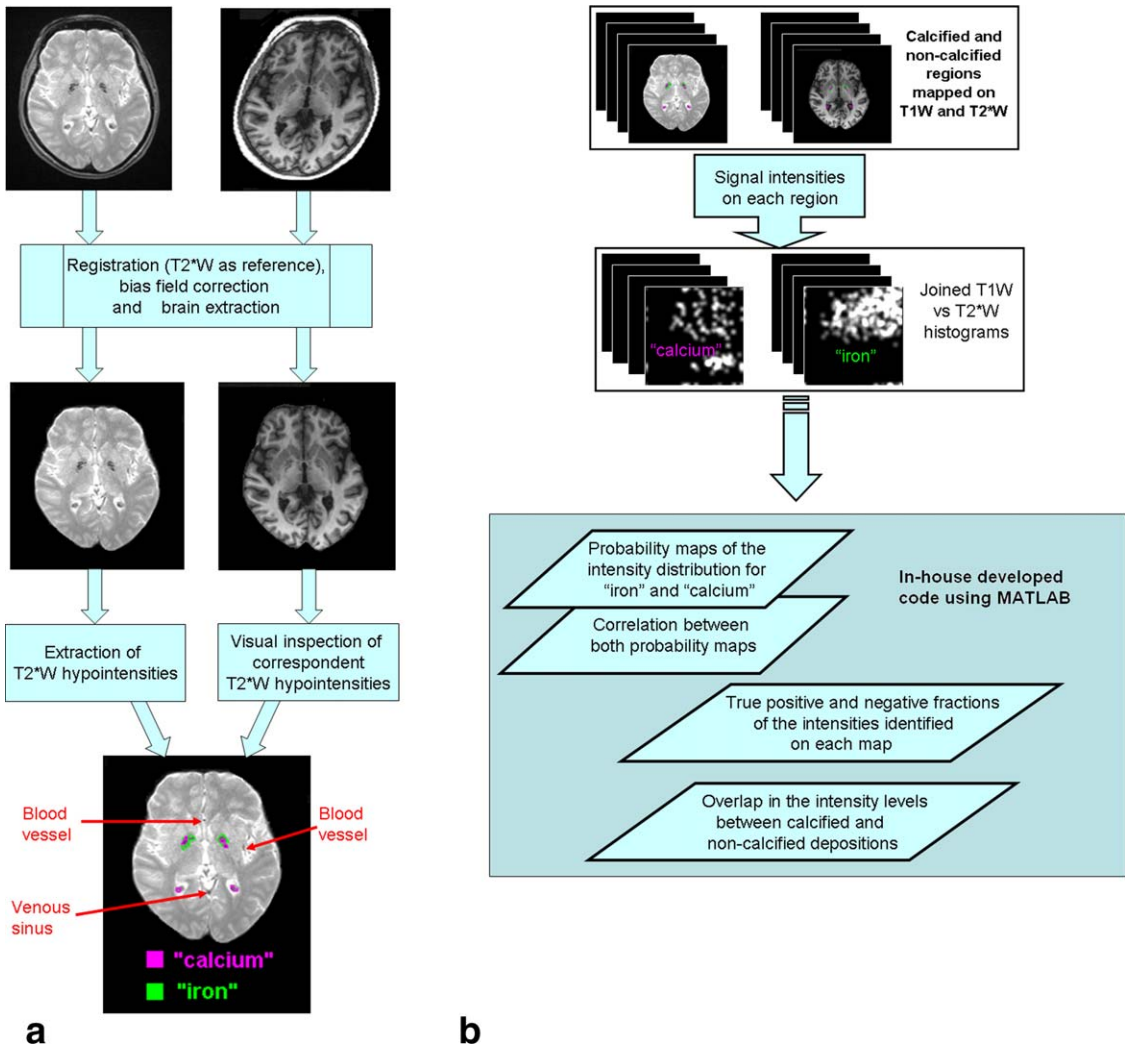

Figure 2. Flow chart of the image processing pipeline. **a:** MRI preprocessing and segmentation of calcified and noncalcified mineral deposits. **b:** Differentiation and relationship between the segmented regions. [Color figure can be viewed in the online issue, which is available at wileyonlinelibrary.com.]

as a reference in accordance with a previous study, which demonstrated that T2*W intensities of the deep gray matter relative to the T2*W intensities of normal appearing white matter resulted in values that correlated well with corresponding R2* (=1/T2*) relaxivity rates (27). The threshold factor n was estimated by adjusting the T2*W threshold so that it lies below most T2*W intensities of normal-appearing globus pallidus tissue, which is the region where T2*W hypointensities are found most often (28). Upon application of the threshold, additional segmented areas automatically detected by the software (eg, blood vessels, isolated voxels near the edges) were scrutinized and identified as false positives to be subsequently deleted.

As both calcified and noncalcified mineral deposits presumed to be iron appear hypointense on T2*W, it was necessary to discern, among the automatically selected regions, which to label as "calcium" or "iron." This was achieved by visually analyzing the segmented regions on the co-registered T1W image. Regions were identified as "iron" if the correspondent region on the T1W image showed no signal change, or "calcium" if the correspondent region on the T1W image was either hypo- or hyper-intense with respect to the mean intensity of the surrounding tissue (7). Iron in the form of methemoglobin can be a limiting factor of this method, because it can also cause an increase in T1W signal due to a reduction in T1 relaxation time. However, the formation of methemoglobin is linked to intra- and extracellular mechanisms that have opposite effects on the T2 relaxation time (29) leading to heterogeneous appearances on T2*W, although such deposits are mainly isointense with respect to the parenchymal tissue, and are, therefore, considered separately if visually identified.

Despite "iron" and "calcium" deposits being mutually exclusive according to the criterion followed for their identification, in some cases, the size of these accumulations and the intensity inhomogeneities on the region (despite previous correction), made it impossible to separate one from the other using the segmentation method. In this case, the region was labeled as having both "iron" and "calcium."

Once the segmentation process for an entire scan was completed, the resulting segmented areas were

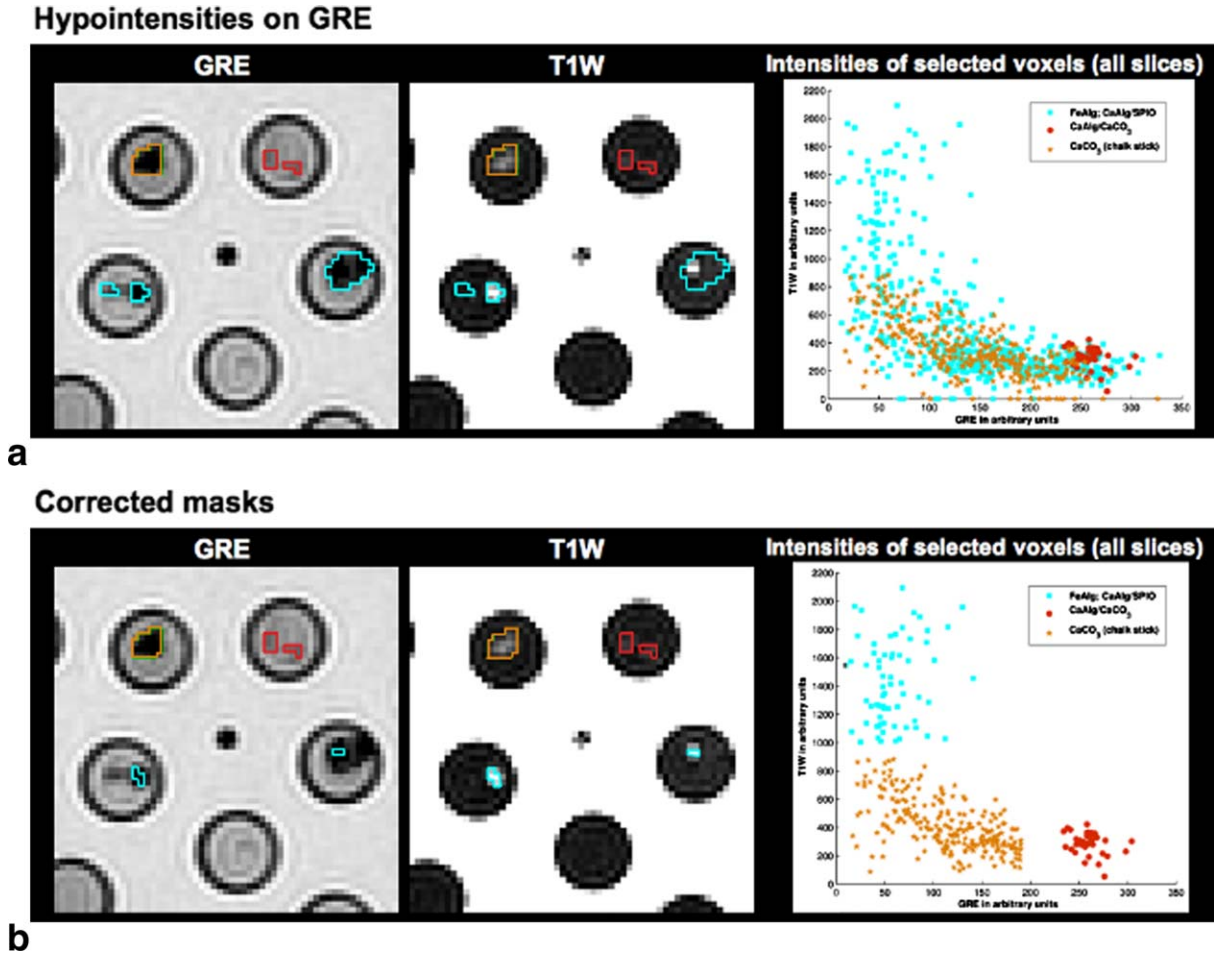

Figure 3. Appearance of calcium and iron deposit models on T2*W and T1W MRI (left and middle columns). **a:** The perimeters of the hypointensity masks, which are cyan for iron deposits, and red and yellow ochre for calcium deposits, are superimposed on a typical slice of the T2*W and T1W phantom images. **b:** The corresponding T2*W and T1W voxel intensities, which are selected by the mineral model masks of all slices, are shown in the scatter plots. The scatter plot at the top and the bottom shows the mineral model voxel intensities selected by the noneroded and eroded mineral model masks, respectively.

saved as binary masks. The minerals' volumes were quantified and expressed in mm^3. Figure 2a summarizes this process.

The hypointensities caused by calcium and iron deposits models were segmented on the T2*W phantom volumes following similar procedure (ie, thresholding combined with a region growing algorithm). In addition, the obtained masks were eroded by 1 voxel to reduce partial volume effects and blurring artifacts, and superimposed onto the T1W images to construct joint scatter plots of T1W and T2*W intensities that were selected by the masks.

Characterization of Potentially Calcified and Noncalcified Mineral Deposits on Brain Scans

The binary masks of each mineral (ie, "iron" and "calcium") were applied to both T1W and T2*W brain images to extract the actual intensity values on both sequences. These were used to generate two-dimensional (2D) joint histograms which were later normalized with the maximum total counts of each mineral. The normalized histograms represented the 2D probability maps of the intensity distribution for each mineral type on the brain scans. We calculated the 2D correlation coefficient, mean and standard deviation of the "iron" and "calcium" 2D probability maps for each subject and the total true positive and negative fractions (ie, excluding the overlap) of the intensities for each mineral map. Treating each map as a 2D array, we reshaped them to vectors to perform the two-sample Kolmogorov-Smirnov test to check if both maps share the same distribution. The similarity between the calcified areas and iron deposits was then measured using Euclidean distance. The pipeline of this process is illustrated in Figure 2b.

To determine the similarity between the T1W and T2*W intensities in regions segmented as "iron" and "calcium" across the whole sample, we generated cross-correlation matrices for both "iron" and "calcium."

Association Between Volumes of Iron Deposits and Calcified Regions on Brain Scans

Associations between volumes of iron deposits and calcified regions were investigated using a univariate linear regression model implemented in SPSS 18.0 (SPSS Inc, Chicago, IL); P values < 0.05 were

Table 1
Mineral Models of the Phantom and Visually Equivalent Brain Iron Deposits as a Consequence of Micro-/Macrohemorrhages*

Phantom substance and reference	Type of brain iron†	Characteristic stage†	Time from occurrence†	Intensity level compared to normal-appearing white matter	
				T1-weighted	T2*-weighted†
CaAlg referred to agarose	Oxy-hemoglobin	Hyperacute	<24 h	Isointense	Slightly hypointense
CaAlg referred to $CuSO_4$/NaCl	Deoxy-hemoglobin	Acute	1–3 days	Slightly hypointense	Very hypointense
	Methemoglobin	Subacute (early)	>3 days	Very hyperintense	Very hypointense
FeAlg referred to agarose	Methemoglobin	Subacute (late)	>7 days	Very hyperintense	Slightly hypointense
CaAlg referred to agarose	Hemichromes/ ferritin	Chronic (center)	>14 days	Isointense	Slightly hypointense
CaAlg referred to $CuSO_4$/NaCl	Hemosiderin	Chronic (rim or small)		Slightly hypointense	Very hypointense
$CaCO_3$ referred to $CuSO_4$/NaCl	Calcified	Chronic	>3 months	Hypointense	Very hypointense

*Correspondences were made after analyzing the signal intensity that each phantom substance produces, and the descriptions on the literature (studies with histological confirmation) of the signal intensities produced by each mineral compound.
†Differentiation according to Bradley (29).

considered statistically significant. Volume of "iron" was the dependent variable while volume of "calcium" was the independent variable. To investigate the influence of head size on the associations, a separate model was developed using the ICV as a covariate.

RESULTS

Phantom

On the T2*W phantom images, FeAlg, CaAlg/SPIO, and $CaCO_3$ appeared very hypointense and CaAlg/$CaCO_3$ slightly hypointense relative to the surrounding agarose. On the T1W phantom images, FeAlg and CaAlg/SPIO appeared more hyperintense than $CaCO_3$ and CaAlg/$CaCO_3$, also relative to the surrounding agarose. CaAlg could not be distinguished from agarose on T2*W sequences and was not analyzed further.

Figure 3a shows the T1W and T2*W scatter plot that was generated with the calcium and iron deposit masks before erosion of one slice and the corresponding scatter plot with all mineral model voxel intensities from the phantom. T1W and T2*W intensities

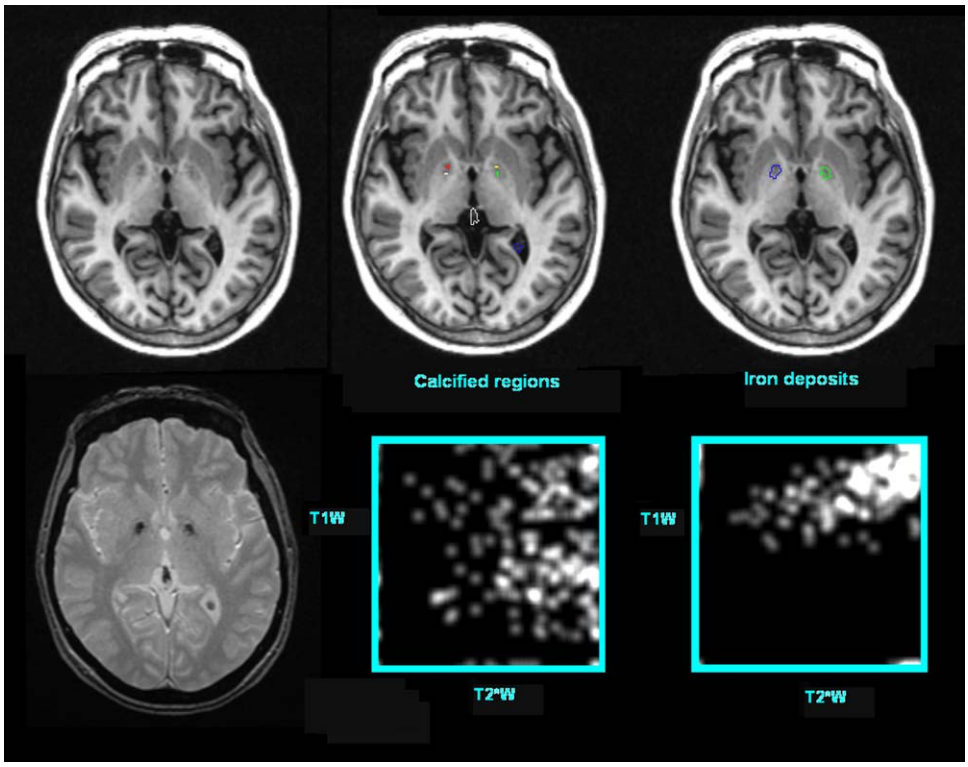

Figure 4. Axial slices of a representative subject showing the segmentations of calcified regions and iron deposits on T1W (upper row) and the joint T1W versus T2*W histograms of the intensities on the segmented regions across all slices in this subject (bottom row). Each region of interest (ROI) (ie, mineral deposit given by one group of connected components) is outlined using a different color. Number of ROIs and total volume of each type of mineral deposition were used to calculate the associations between both types of mineral depositions. [Color figure can be viewed in the online issue, which is available at wileyonlinelibrary.com.]

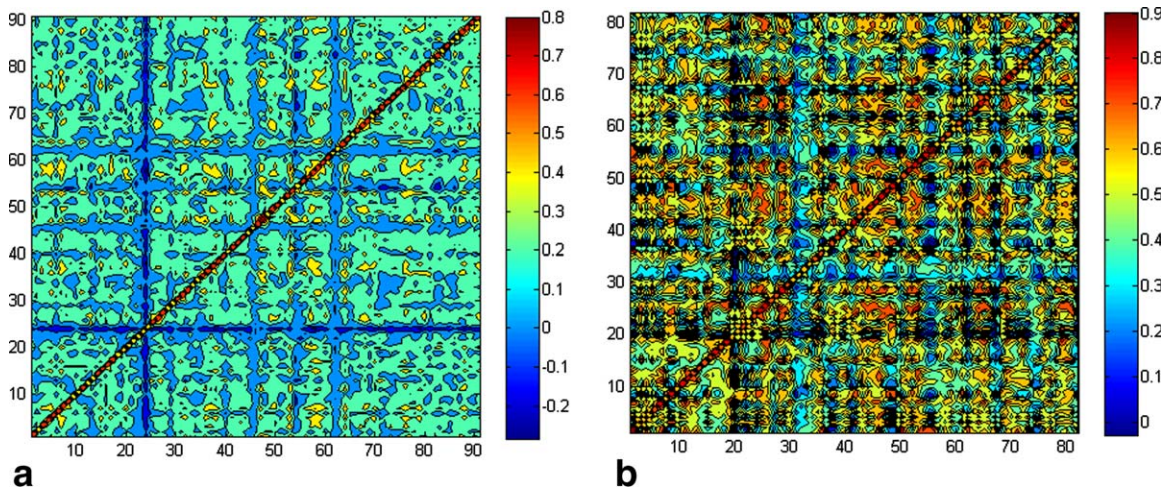

Figure 5. Cross-correlation matrices of the joint histograms: calcified regions (a) and iron deposits (b). Observe the magnitude of the correlation between subjects. It is more than 0.5 for the iron deposits and generally less than 0.4 for the calcified regions. Observe that as these are cross-correlation matrices, all elements in the principal diagonal are equal to 1. [Color figure can be viewed in the online issue, which is available at wileyonlinelibrary.com.]

from voxels of $CaCO_3$ (yellow ochre) and CaAlg/$CaCO_3$ (red) form distinct clusters whereas intensities from FeAlg and CaAlg/SPIO voxels (cyan) form a cloud that overlaps significantly with the first two clusters. Figure 3b shows the T1W and T2*W scatter plot that was generated with the calcium and iron deposit mask, which selected all focal hyperintensities on the T1W phantom volume and hence did not select regions on T2*W volumes that were affected by the partial volume effect and blurring artifacts. Here all three clusters can clearly be distinguished in the corresponding scatter plot. Importantly, the scatter plot shows that T1W intensities clearly differentiate calcium and iron deposits. Table 1 summarizes how the visual appearance of mineral models of the phantom potentially relates to the visual appearance of mineral deposits in the brain.

Subjects

Iron deposits were identified in 82/100 datasets, calcified regions in 91/100 and both types in 77/100. Examples of the segmentation can be seen in Figure 4. After segmentation, the volumes of "iron" (n = 100; mean = 283.76 mm^3; SD = 581.51 mm^3) and "calcium" (n = 100; mean = 236.74 mm^3; SD = 309.70 mm^3) were both normally distributed across the sample.

The 2D correlation coefficients between the T1W versus T2*W intensity maps, one for "iron" and one for "calcium" for each subject, and the true positive and negative fractions for each distribution are summarized in Table 2. The mean Euclidean distance between the probability maps of iron and calcium was statistically different from 0 (t = 16.934; $P < 0.001$). Figure 5 shows the cross-correlation matrices of the joint histograms of T1W and T2*W for the iron deposits and calcified regions across the sample. In general, better agreement between the T1W/T2*W intensities was found (higher cross-correlation) in the regions identified as iron deposits, than in those labeled as calcified regions. The two-sample Kolmogorov-Smirnov revealed that on only one subject (from the 77 subjects who had both types of mineral depositions) the intensity distributions of the joint histograms for "iron" and "calcium" was the same (null hypothesis). On the remaining 76 subjects, the null hypothesis was rejected at the 5% significance level.

The regression analysis showed that greater iron accumulation was associated with greater calcium accumulation (n = 100; standardized $\beta = 0.319$; $P < 0.005$). The same analysis was also performed after excluding the scans with no detectable "iron" or "calcium," allowing examination of the association between their accumulations only in those subjects with both types of mineral deposits. For this analysis,

Table 2
Results of the Intensity Analysis of Both Features: Iron Deposits and Calcified Regions

	2D correlation between maps of iron deposits and calcified regions	True positive fraction		True negative fraction	
		Iron deposits	Calcified regions	Iron deposits	Calcified regions
Average	0.266	0.993	0.995	0.899	0.878
Minimum	0.021	0.961	0.947	0.499	0.405
Maximum	0.859	0.999	0.999	0.998	0.997
SD	0.166	0.006	0.006	0.105	0.123
CI (alpha 0.95)	0.001	4.7e-05	4.7e-05	0.0007	0.0008

CI = confidence interval, SD = standard deviation.

Table 3
Associations Between Volumes of Iron Deposits and Volumes of Calcified Regions in Brains of Participants Grouped According to the Location Where the Mineral Accumulation Was Observed

Location	Brains with iron deposits and calcified regions in	Brains with iron deposits only in	Brains with calcified regions only in	Brains with calcified regions in	Brains with iron deposits in
Basal ganglia	**β = 0.410** $P = 0.034$ n = 27	**β = 0.303** $P = 0.031$ n = 51	β = n.a. P = n.a. n = 2	β = 0.352 $P = 0.061$ n = 29	**β = 0.323** $P = 0.004$ n = 76
Choroid plexus	β = n.a. P = n.a. n = 2	β = n.a. P = n.a. n = 1	**β = 0.392** $P = 0.0002$ n = 85	**β = 0.386** $P = 0.0002$ n = 87	β = n.a. P = n.a. n = 3
Elsewhere*	β = n.a. P = n.a. n = 2	β = 0.176 $P = 0.391$ n = 26	β = n.a. P = n.a. n = 3	β = n.a. P = n.a. n = 7	β = 0.285 $P = 0.127$ n = 30
Same place (regardless)	**β = 0.526** $P = 0.002$ n = 31				
Elsewhere* (iron deposits &/ or calcified regions)†	β = 0.264 $P = 0.138$ n = 33				

β values are the standardized coefficients. n.a. = not applicable (due to small sample size).
*Elsewhere includes the brainstem, gray matter, and corpus callosum.
†Scans used here will have either "calcium" or iron, or both "calcium" and iron in any number of locations defined above.

the association was similar (n=77; β = 0.368; $P < 0.001$). Correcting for ICV in the model, as expected, did not change the association between "iron" and "calcium" accumulation.

The location-based analysis (Table 3) showed that iron deposits were mainly found in the basal ganglia, whereas calcified regions were mainly identified in the choroid plexus. The association between the volumes of the calcified regions and those of iron deposits was highest in scans where both were identified in the same anatomical region (β=0.526; $P < 0.005$).

DISCUSSION

Mineral depositions that predominantly consist of iron or calcium can be detected and differentiated from each other on conventional clinically available MRI sequences. The framework proposed to examine the relationship between mineral accumulations using conventional structural MRI identified distinct intensity distributions for the two predominant mineral depositions analyzed. A novel MRI phantom containing calcium and iron deposits supported our hypothesis that calcified regions produce a signal change in T1W images that allows them to be differentiated from deposits where iron is prevalent; both are known to appear hypointense on T2*W images. These results are in agreement with studies that had histological confirmation, two of which reported that calcium and other minerals appear hyperintense on T1W (24,30), three studies that reported that calcium and hemosiderin appear hypointense on T1W (31–33), and other three studies, which reported that noncalcified regions appear isointense on T1W (34–36).

The higher cross-correlation in the joint T1W versus T2*W histograms of the brain regions identified as iron deposits compared with those labeled as calcified regions suggests that, although there is an unavoidable overlap between both regions, deposits of iron macromolecules alone cause a more definable signal change on T1W and T2*W sequences than when there are other mineral aggregates sharing the same physical region. This, therefore, suggests that the automatic segmentation of iron deposits can be achieved more easily than calcified regions. This is expected, due to the high dispersion in the intensities in calcified regions.

Although the subjects selected for this study and the study design do not allow us to generalize the pattern of mineral accumulation in a general healthy ageing population, our findings support our initial hypothesis that there is a positive correlation between the accumulation of iron and calcified regions, regardless of whether the individuals have both types of mineral accumulations or only one of them, and associations are higher when both types of deposits occur in the same region. A shared pathway of iron and calcium has been suggested for the age-related deposition in the brain, based on findings of multiple minerals accumulating in the same deposit. This sometimes has been attributed initially to only one mineral in the brain (15,37) and other times to a shared transporting mechanism as both minerals are present in the serum, with iron transferred to tissues from the blood (38) and calcium in its bound form leading to calcification of blood vessels (39).

The strengths of this study are: (i) the sample was deliberately chosen to represent a wide spectrum of mineral loads and imaging features commonly present in an ageing population, (ii) the combined use of a phantom and in vivo images acquired using the same imaging protocol and (iii) the same scanner to validate the signal characteristics of each type of mineral deposition, and (iv) the intensity-based statistical framework devised here. The latter could be useful for discerning whether, in medical imaging, two features of similar intensity levels on one or more MR sequences can be distinguished one from each other using a given segmentation method.

One limitation of this study is the use of an assessment technique (ie, thresholding on magnitude images, followed by manual removal of false positives) that, despite having a high sensitivity, is observer-dependent (40) and affected by blooming artifacts. However, a single analyst used the same thresholding method to generate masks for all subjects of the sample, and the manual removal of false positives was consistently restricted only to single isolated voxels and voxels of the boundaries of the brain parenchyma in all cases. The blooming artifact has been recognized to affect the assessment of T2*W hypointensities (28), once it is not uniform (ie, does not increase the size of all T2*W hypointensities in the same proportion) (41) and depends on the susceptibility of the magnetic particles (42) — given that for our case the field strength and sequence parameters, which also influence this artifact, were the same. As myelin has overwhelming negative effects on the correlation between R2* and iron concentrations (43), it is possible that the blooming artifact is also influenced by the location of the T2*W hypointensities. The majority of the mineral depositions were found in regions of cortical/subcortical gray matter (of lower myelin content), being calcified regions particularly concentrated in the choroid plexus. Therefore, the blooming artifact, and hence the threshold, was mainly influenced by the magnetic susceptibility of the particles that caused the hypointensities, and consequently by the degradation stage of the iron particles and their proportion with respect to the other minerals aggregated in the named "calcified" regions. While in one third of the sample, iron deposits and calcified regions spatially overlapped, it was possible to identify two distinct intensity distributions for the regions extracted and differentiated with the proposed technique.

Another potential limitation is that this study was performed only at 1.5T. However, despite these limitations, our results are in agreement with previous reports on location of iron deposits and calcified regions obtained from studies that had histological confirmation (7,37). Other studies that assessed iron deposition at different magnetic fields (from 0.5T to 4.7T) report a decrease on T2W for hemosiderin at higher magnetic fields and an increased ratio in T1/T2 for ferritin with increasing field strengths (44,45). Studies that used T2*W MRI have reported the appearance of iron and calcified regions consistently hypointense at different field strengths (13). Therefore, our findings could also be transferred to images obtained at other magnetic field strengths.

Further research should focus on developing fully automated and reliable techniques for quantifying both types of mineral deposits on sequences used on routine clinical practice. Optimally, such algorithms should consider deriving the threshold for identifying these deposits from quantitative parameters (eg, relaxation rate mapping). This could be of great importance to determine the role that mineral deposits, specially calcium and iron, play in other metabolic processes, cerebrovascular mechanisms, brain functioning and cognition.

ACKNOWLEDGMENTS

We thank the study participants; Catherine Murray for work on recruitment; and nurses, radiographers and other staff at the Brain Research Imaging Centre, Edinburgh. This work was funded by Age UK and the UK Medical Research Council as part of the project "Disconnected Mind: LBC1936" (http://www.disconnectedmind.ed.ac.uk/) (including the Sidney De Haan Award for Vascular Dementia), the Centre for Cognitive Ageing and Cognitive Epidemiology (http://www.ccace.ed.ac.uk/), Row Fogo Charitable Trust and SINAPSE (Scottish Imaging Network A Platform for Scientific Excellence) collaboration, with additional funding from the Biotechnology and Biological Sciences Research Council, the Engineering and Physical Sciences Research Council and the Economic and Social Research Council. A.J.K. is funded by The University of Edinburgh College of Medicine Vacation Scholarship, A.G. and D.A.D. are funded by SINAPSE-SPIRIT PhD Scholarships and JMW is partially funded by SINAPSE.

REFERENCES

1. Rivera-Mancía S, Pérez-Neri I, Ríos C, Tristán-López L, Rivera-Espinosa L, Montes S. The transition metals copper and iron in neurodegenerative diseases. Chem Biol Interact 2010;186:184–199.
2. Brewer GJ. Risks of copper and iron toxicity during aging in humans. Chem Res Toxicol 2010;23:319–326.
3. Yu JT, Chang RC, Tan L. Calcium dysregulation in Alzheimer's disease: from mechanisms to therapeutic opportunities. Prog Neurobiol 2009;89:240–255.
4. Hallgren B, Sourander P. The effect of age on the non-haemin iron in the human brain. J Neurochem 1958;3:41–51.
5. Penke L, Valdés Hernández MC, Muñoz Maniega S, et al. Brain iron deposits are associated with general cognitive ability and cognitive aging. Neurobiol Aging 2012;33; 510–517.
6. Office for National Statistics. Life expectancy: life expectancy continues to rise. London: UK National Statistics, Health, Life Expectancy; 2010.
7. Ropele S, de Graaf W, Khalil M, et al. MRI assessment of iron deposition in multiple sclerosis. J Magn Reson Imaging 2011;34:13–21.
8. Kida K, Kajitani T, Goto S, Tsuji Y, Maruyama T, Azuma Y.Detection of calcification using high-pass filtered phase image in magnetic resonance imaging for breast cancer screening. In: Proceedings of the 2011 IEEE International Conference on Imaging Systems and Techniques, Batu Ferringhi, Penang, Malaysia, 2011. [full-paper ISBN 978-1-61284-896-9/11].
9. Cusack R, Papadakis N. New robust 3D phase unwrapping algorithms: application to magnetic field mapping and undistorting echoplanar images. Neuroimage 2002;16:754–764.
10. Roemer PB, Edelstein WA, Hayes CE, Souza SP, Mueller OM. The NMR phase array. Magn Reson Med 1990;16:192–225.
11. Hammond KE, Lupo JM, Xu D, et al. Development of a robust method for generating 7.0T multichannel phase images of the brain with application to normal volunteers and patients with neurological diseases. Neuroimage 2008;39:1682–1692.
12. Bernstein MA, Grgic M, Brosnan TJ, Pelc NJ. Reconstructions of phase contrast, phased array multicoil data. Magn Res Med 1994;32:330–334.
13. Valdés Hernández MC, Maconick LC, Tan EJM, Wardlaw JM. Identification of mineral deposits in the brain on radiological images. Eur Radiol 2012;22:2371–2381.
14. Kruer MC, Boddaert N, Schneider SA, et al. Neuroimaging Features of Neurodegeneration with Brain Iron Accumulation. AJNR Am J Neuroradiol 2012;33:407–414.
15. Harder SL, Hopp KM, Ward H, Neglio G, Gitlin J, Kido D. Mineralization of the deep gray matter with age: a retrospective review

with susceptibility-weighted MR imaging. AJNR Am J Neuroradiol 2008;29:176–183.
16. Price RR, Axel L, Morgan T, et al. Quality assurance methods and phantoms for magnetic resonance imaging: report of AAPM nuclear magnetic resonance Task Group No. 1. Med Phys 1990; 17:287–295.
17. Henkelman R, Watts J, Kucharczyk W. High signal intensity in MR images of calcified brain tissue. Radiology 1991;179:199–206.
18. Draget KI, Smidsrod O, Skjåk-Bræk G. Alginates from algae. In: Biopolymers Online, Wiley Online Library 2005.
19. Deary IJ, Gow AJ, Taylor MD, et al. The Lothian Birth Cohort 1936: a study to examine influences on cognitive ageing from age 11 to age 70 and beyond. BMC Geriatr 2007;7:28.
20. Wardlaw JM, Bastin ME, Valdés Hernández MC, et al. Brain ageing, cognition in youth and old age, and vascular disease in the Lothian Birth Cohort 1936: rationale, design and methodology of the imaging protocol. Intl J Stroke 2011;6:547–559.
21. Ramirez J, Gibson E, Quddus A, et al. Lesion Explorer: a comprehensive segmentation and parcellation package to obtain regional volumetrics for subcortical hyperintensities and intracranial tissue. Neuroimage 2011;54:963–973.
22. Tustison NJ, Avants BB, Cook PA, et al. N4itk: improved n3 bias correction. IEEE Trans Med Imaging 2010;29:1310–1320.
23. Valdés Hernández MC, Royle NA, Jackson MR, et al. Color fusion of Magnetic Resonance Images improves intracranial volume measurement in studies of ageing. O J Rad 2012;2:1–9. doi: 10.4236/ojrad.2012.21001
24. Higano S, Takahashi S, Kurihara N, et al. Supratentorial primary intra-axial tumors in children. MR and CT evaluation. Acta Radiol 1997;38:945–952.
25. Patenaude B, Smith SM, Kennedy D, Jenkinson M. A Bayesian model of shape and appearance for subcortical brain. Neuroimage 2011;56:907–922.
26. Glatz A, Valdés Hernández MC, Kiker AJ, et al. Automatic segmentation of basal ganglia iron deposits from structural MRI. MIUA 2011, On-line Proceedings. http://www.biomedical-image-analysis.co.uk/images/stories/glatz-posters1-32.pdf Accessed August 15, 2013.
27. Yan SQ, Sun JZ, Yan YQ, Wang H, Lou M. Evaluation of brain iron content based on magnetic resonance imaging (MRI): comparison among phase value, R2* and magnitude signal intensity. PloS One 2012;7:e31748.
28. Glatz A, Valdés Hernández MC, Kiker AJ, Bastin ME, Deary IJ, Wardlaw JM. Characterization of multifocal T2*-weighted MRI hypointensities in the basal ganglia of elderly, community-dwelling subjects. Neuroimage 2013;82C:470–480.
29. Bradley WG. MR appearance of hemorrhage in the brain. Radiology 1993;189:15–26.
30. Maeda H, Sato M, Yoshikawa A, et al. Brain MR imaging in patients with hepatic cirrhosis: relationship between high intensity signal in basal ganglia on T1-weighted images and elemental concentrations in brain. Neuroradiology 1997;39:546–550.
31. Akutsu H, Tsuboi K, Sakamoto N, Nose T, Honma S, Jikuya T. Cerebral metastasis from angiosarcoma of the aortic wall: case report. Surg Neurol 2004;61:68–71.
32. Morita H, Ikeda S, Yamamoto K, et al. Hereditary ceruloplasmin deficiency with hemosiderosis: a clinicopathological study of a Japanese family, Ann Neurol 1995;37:646–656.
33. Vymazal J, Righini A, Brooks RA, et al. T1 and T2 in the brain of healthy subjects, patients with Parkinson disease, and patients with multiple system atrophy: relation to iron content. Radiology 1999;211:489–495.
34. Curtis AR, Fey C, Morris CM, et al. Mutation in the gene encoding ferritin light polypeptide causes dominant adult-onset basal ganglia disease. Nat Genet 2001;28:350–354.
35. El Tannir El Tayara N, Delatour B, et al. Age-related evolution of amyloid burden, iron load, and MR relaxation times in a transgenic mouse model of Alzheimer's disease. Neurbiol Dis 2006;22: 199–208.
36. Ogg RJ, Steen RG. Age related changes in brain T1 are correlated with putative iron concentration. Magn Reson Med 1998;40:749–753.
37. Casanova MF, Araque JM. Mineralization of the basal ganglia: implications for neuropsychiatry, pathology and neuroimaging. Psychiatry Res 2003;121:59–87.
38. Haacke EM, Makki M, Ge Y, et al. Characterizing iron deposition in multiple sclerosis lesions using susceptibility weighted imaging. J Magn Reson Imaging 2002;29:537–544.
39. Ramonet D, Pugliese M, Rodríguez MJ, et al. Calcium precipitation in acute and chronic brain diseases. J Physiol Paris 2002; 96:307–312.
40. Valdés Hernández MC, Jeong TH, Murray C, et al. Reliability of two techniques for assessing cerebral iron deposits with structural Magnetic Resonance Imaging. J Magn Reson Imaging 2011; 33:54–61.
41. De Reuck J, Auger F, Cordonnier C, et al. Comparison of 7.0-T T2*-magnetic resonance imaging of cerebral bleeds in post-mortem brain sections of Alzheimer patients with their neuropathological correlates. Cerebrovasc Dis 2011;31:511–517.
42. Pintaske J, Müller-Bierl B, Schick F. Geometry and extension of signal voids in MR images induced by aggregations of magnetically labelled cells. Phys Med Biol 2006;51:4707–4718.
43. Langkammer C, Krebs N, Goessler W, et al. Susceptibility induced gray-white matter MRI contrast in the human brain. Neuroimage 2012;59:1413–1419.
44. Vymazal J, Brooks RA, Baumgarner C, et al. The relation between brain iron and NMR relaxation times: an in vitro study. Magn Reson Med 1996;35:56–61.
45. Hocq A, Brouette N, Saussez S, Luhmer M, Gillis P, Goussin Y. Variable-field relaxometry of iron-containing human tissues: a preliminary study. Contrast Media Mol Imaging 2009;4:157–164.